

## A Coupled-Pixel Model (CPM) Atmospheric Retrieval Algorithm for High-Resolution Imagers

MARY MORRIS AND CHRISTOPHER S. RUF

*University of Michigan, Ann Arbor, Michigan*

(Manuscript received 16 January 2015, in final form 8 July 2015)

### ABSTRACT

Low-frequency passive microwave observations allow for oceanic remote sensing of surface wind speed and rain rate from spaceborne and airborne platforms. For most instruments, the modeling of contributions of rain absorption and reemission in a particular field of view is simplified by the observing geometry. However, the simplifying assumptions that can be applied in most applications are not always valid for the scenes that the airborne Hurricane Imaging Radiometer (HIRAD) regularly observes. Collocated Stepped Frequency Microwave Radiometer (SFMR) and HIRAD observations of Hurricane Earl (2010) indicate that retrieval algorithms based on the usual simplified model, referred to here as the decoupled-pixel model (DPM), are not able to resolve two neighboring rainbands at the edge of HIRAD's swath. The DPM does not allow for the possibility that a single column of atmosphere can affect the observations at multiple cross-track positions. This motivates the development of a coupled-pixel model (CPM) that is developed and tested in this paper. Simulated observations as well as HIRAD's observations of Hurricane Earl (2010) are used to test the CPM algorithm. Key to the performance of the CPM algorithm is its ability to deconvolve the cross-track scene, as well as unscramble the signatures of surface wind speed and rain rate in HIRAD's observations. While the CPM approach was developed specifically for HIRAD, other sensors could employ this method in similar complicated observing scenarios.

### 1. Introduction

Since the 1970s, airborne and spaceborne passive microwave radiometers have provided scientists with observations of the emission from the ocean and atmosphere (Wilheit 1976; Weinman and Guetter 1977; Prabhakara et al. 1992). Signatures of rain and wind exist in low-frequency microwave observations because rain absorbs and reemits radiation (Wilheit 1986) and wind-driven sea foam enhances the emission from the sea surface (Stogryn 1967; Nordberg et al. 1971; Rosenkranz and Staelin 1972). Today, spaceborne satellite missions like TRMM and GPM employ Bayesian algorithms to instantaneously retrieve rain rate with databases built offline (Kummerow et al. 1996). At the aircraft level, the Stepped Frequency Microwave Radiometer (SFMR) is used to estimate surface wind speed and rain rate in tropical cyclones. SFMR's C-band

observations allow for tropical cyclone–strength surface wind speed retrieval, after correcting for heavy rain absorption (Uhlhorn et al. 2007; Klotz and Uhlhorn 2014).

Most airborne and spaceborne sensors have observing geometries that allow for simplifying assumptions when modeling the rain that is present in their fields of view (Uhlhorn et al. 2007; Kummerow et al. 1996). The rain is assumed to exist only below the freezing level of the atmosphere. Figure 1a shows the observing geometry of a typical spaceborne imaging radiometer. The horizontal extent of individual pixels in the image is indicated by vertical tick marks along the black surface boundary. The region of the atmosphere that contributes to a measurement at a particular pixel is indicated by the expanding conic boundary away from the sensor, denoted in Fig. 1 by striped polygons. The dispersion of the cone is determined by the angular resolution of the sensor. Highlighted in yellow in Fig. 1a is the part of the rain column that contributes to the downwelling and not the upwelling thermal emission measured at a particular pixel, but would however contribute to the upwelling thermal emission in the neighboring pixel. The adjacent

---

*Corresponding author address:* Mary Morris, Dept. of Climate and Space Sciences and Engineering, University of Michigan, 2455 Hayward St., Ann Arbor, MI 48109-2143.  
E-mail: marygm@umich.edu

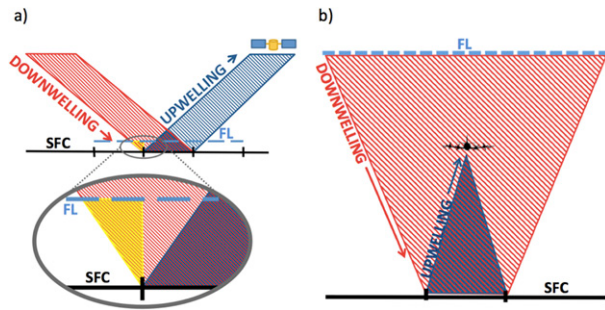


FIG. 1. Typical observing geometry of (a) a spaceborne microwave radiometer and (b) the airborne SFMR (not to scale), where FL stands for freezing level, and SFC stands for Earth surface. The yellow shaded region on the left represents the relatively small portion of the rain column below the freezing level that is not common to both the upwelling and downwelling emission sensed by the radiometer. The horizontal extent of individual pixels in the image is indicated by black vertical tick marks.

portion of the rain column that contributes to both the upwelling and downwelling emission can be seen to be much greater. This is a direct result of the fact that the horizontal resolution of the imager's pixels is significantly greater than the height of the freezing level. This condition is common with spaceborne radiometer imagers and is the reason why the radiative transfer models typically used in these applications assume that the upwelling and downwelling atmospheric emission originates from the same atmospheric column (Stephens and Kummerow 2007; Wilheit et al. 1994).

Simplifying assumptions about rain along the propagation path can also be made for an airborne radiometer like SFMR, but for different reasons. SFMR is a nadir-looking radiometer with horizontal resolution on the order of typical convective rain cell features, which is smaller than most stratiform rain distributions (Uhlhorn and Black 2003). Figure 1b illustrates the relative contributions of the atmosphere below the freezing level for this airborne-observing geometry. In this case, a larger portion of the downwelling propagation path spills over into the next surface pixel. However, since large gradients in rain—on the order of  $10 \text{ mm h}^{-1} \text{ km}^{-1}$ —are unlikely at this horizontal scale, rain in the spillover region can be assumed to be similar to the rain in the main pixel of observation.

There are certain conditions under which the simplifying assumptions mentioned above are no longer valid. While developing a physically based retrieval algorithm for the Hurricane Imaging Radiometer (HIRAD), these assumptions failed often. HIRAD was developed with the goal of achieving SFMR-observing capabilities over a wider cross-track swath; therefore, initial retrieval algorithm development for HIRAD was based on established SFMR algorithms (Amarin et al. 2012).

However, approximations that are reasonable given SFMR's nadir-viewing geometry become much less valid for HIRAD's nonnadir pixels, especially at the higher incidence angle portions of its swath edge and in a tropical cyclone environment.

Collocated HIRAD/SFMR observations of Hurricane Earl (2010) during GRIP (Braun et al. 2013) exposed the flaws in using SFMR-like assumptions in the forward radiative transfer model on which HIRAD's retrieval algorithm is based. HIRAD and SFMR were on separate aircraft, flying perpendicular to one another. HIRAD was flying north on a WB-57 at roughly 20 km in altitude, with Hurricane Earl's western eyewall to its right. SFMR was observing from a NOAA P-3 at roughly 3 km and flew directly over the same western eyewall going from east to west. In this instance, SFMR's nadir observations were able to identify two neighboring, but distinct, rainbands as it flew directly over them. HIRAD, on the other hand, was not able to distinguish between the two when they were imaged at the outer edge of its field of view.

The simplified radiative transfer model used by SFMR and by typical spaceborne radiometer retrieval algorithms, in which each surface pixel has associated with it a single atmospheric column that is directly above it and is responsible for both upwelling and downwelling emission and absorption, will be referred to here as the decoupled-pixel model (DPM). It is decoupled in the sense that the atmosphere observed at each pixel is assumed to be independent of that at any other pixel, so that retrieval algorithms can independently solve for surface and atmospheric state variables at each pixel. A coupled-pixel model (CPM) is developed here that explicitly accounts for the possibility that upwelling and downwelling emission and absorption at a single pixel can result from different portions of the atmosphere, and that a given portion of the atmosphere can affect measurements at multiple pixels in the image. In this case, a corresponding retrieval algorithm will need to couple its geophysical state estimates across multiple pixels in the image.

Since HIRAD regularly observes tropical cyclone conditions in the outermost incidence angles of its large cross-track swath, a new retrieval algorithm was developed based on the CPM. A key feature of the CPM algorithm is that it is able to deconvolve the cross-track scene, as well as unscramble the signatures of surface wind speed and rain rate in HIRAD's observations. While HIRAD will benefit directly from this method, the CPM algorithm approach could potentially be used in other applications and with other sensors, in cases where the horizontal resolution of the imager is comparable to or less than the depth of the atmospheric

column within which a significant portion of the atmospheric attenuation and emission originates.

The objectives of this paper are to present the CPM algorithm and compare its performance to that of the DPM. We hypothesize that the performance will be comparable in conditions without significant horizontal variability in the rain at the scale size of the HIRAD spatial resolution and better in highly variable conditions, such as a double rainband. To begin, section 2 highlights key differences in the forward radiative transfer models used in the DPM and CPM methods. Section 3 outlines the set of simulated observations used to test the CPM algorithm. Section 4 describes the CPM algorithm. Results of the CPM performance tests are reported in section 5. Finally, a discussion of these results is summarized in section 6 and concluded upon in section 7.

## 2. Decoupled and coupled forward radiative transfer models

The appropriate radiative transfer forward model to use given HIRAD's observing geometry depends on assumptions about the atmosphere along the propagation path. A typical situation for off-nadir pixels in the HIRAD image is shown in Fig. 2. Regions 1 and 5 in the figure are modeled as a rain-free gaseous atmosphere above the freezing level. Below the freezing level, where rain may be present, region 2 is the downwelling-only portion of the propagation path, region 3 is the overlapping area of both upwelling and downwelling portions of the path, and region 4 is the upwelling-only portion of the path.

Figure 2a illustrates how the forward radiative transfer model (FRTM) considers the atmosphere under the DPM assumption. The rain in the downwelling path is assumed to be the same as that in the upwelling path. In cases of significant horizontal nonuniformity in the rainfall, such as near the tropical cyclone (TC) eyewall, this assumption may not be valid.

Figure 2b highlights the differences in the FRTM under a CPM assumption. The downwelling and upwelling atmospheres are considered separately, without, for example, assuming that the rain in region 3 is the same as that in region 2 or 4. Note also that the atmosphere along the upwelling and downwelling paths that are associated with a particular surface pixel also pass over other surface pixels. For example, the downwelling path in Fig. 2b passes over three surface pixels, while the upwelling path passes over two. The footprint of these pixels is dependent on the horizontal resolution of the sensor, which is detailed in Amarin (2010).

The appropriate FRTM in this case first requires that the total optical depth along the upwelling and

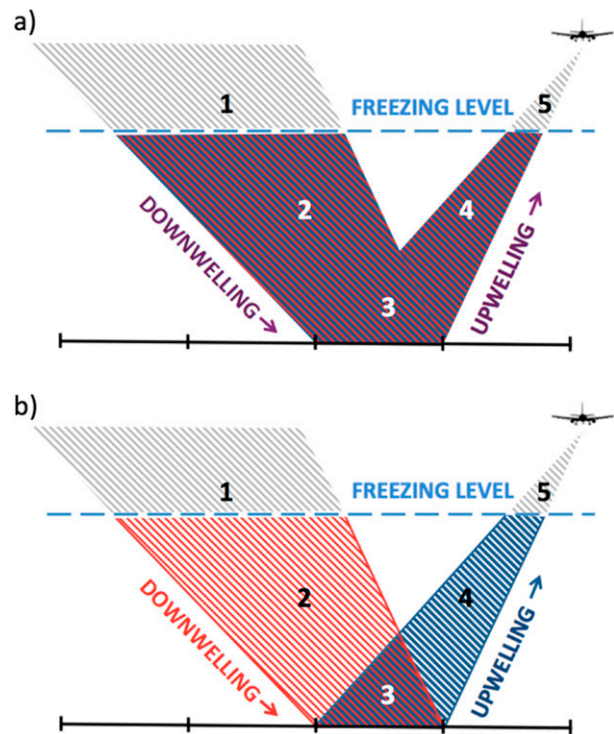


FIG. 2. Diagram showing the assumptions made about the below-freezing-level atmosphere in a DPM (a) vs CPM and (b) forward model. The horizontal extent of individual pixels in the image is indicated by black vertical tick marks. Regions 1 and 5 are modeled as a gaseous atmosphere without rain. Region 2 is the downwelling-only portion of the observing path for a particular field of view. Region 3 is the overlapping area of upwelling and downwelling portions of the path. Region 4 is the upwelling only portion of the path. In (a) in the DPM model, regions 2–4 are modeled assuming the upwelling and downwelling paths have the same rain. In (b) in the CPM model, there is no longer an assumption that the same rain is seen along the upwelling and downwelling paths. While there is a small portion of overlap in the paths (region 3), regions 2 and 4 are not assumed to have the same rain as region 3.

downwelling paths,  $\tau_{UP}$  and  $\tau_{DN}$ , respectively, be calculated from the total rain column that is present along each propagation path. The total is calculated by weighting and summing the rain rate above each pixel according to the cross-sectional volume of atmosphere that the path cuts through below the freezing level (see the appendix for details). Once the two optical depths are calculated, the corresponding upwelling and downwelling brightness temperatures (TBs) are determined similar to Amarin (2010) with (1) and (2), respectively:

$$T_{UP} = \int_0^{TOA} \alpha(z) T(z) \sec(\theta) e^{-\int_z^{TOA} \alpha(z') \sec(\theta) dz'} dz, \quad (1)$$

$$T_{DN} = \int_0^{TOA} \alpha(z) T(z) \sec(\theta) e^{-\int_0^z \alpha(z') \sec(\theta) dz'} dz, \quad (2)$$

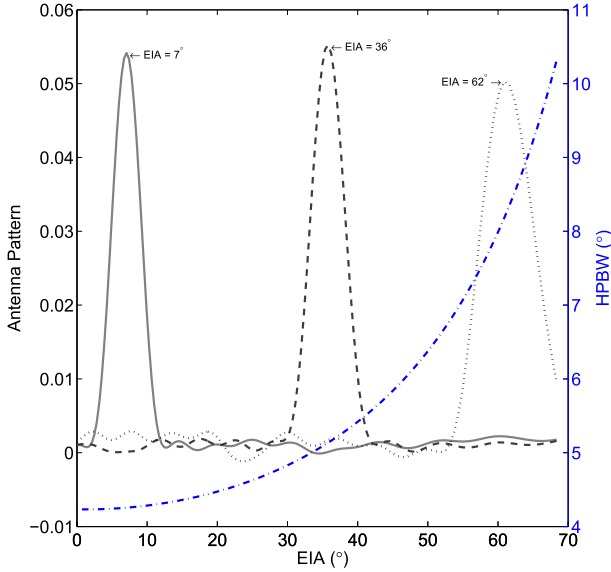


FIG. 3. The relationship between HIRAD's beamwidth and synthetic antenna pattern with EIA. Portions of the synthetic antenna beam patterns are shown in grayscale for EIA of  $7^\circ$ ,  $36^\circ$ , and  $62^\circ$ , and are labeled in the figure. Plotted in blue is the HPBW. HPBW is the angle between points in the antenna pattern where the power is half of the maximum.

where  $\alpha$  is the absorption coefficient;  $T$  is the physical temperature (K);  $z$  is the height in the atmosphere; TOA is the top of the atmosphere, which is assumed to be 20 km in this application; and  $\theta$  is the Earth incident angle (EIA). The observed TB, including atmospheric emission and attenuation as well as surface emission and reflection, is modeled as

$$T_B = T_{UP} + e^{-\tau_{UP}}[\varepsilon T_{SFC} + (1 - \varepsilon)(e^{-\tau_{DN}} T_{COS} + T_{DN})], \quad (3)$$

where  $T_{SFC}$  is the physical sea surface temperature,  $\varepsilon$  is the emissivity of the sea surface, and  $T_{COS}$  is the cosmic microwave background TB. The total path-integrated transmissivity is represented in (3) for the individual upwelling and downwelling propagation paths as  $e^{-\tau_{UP}}$  and  $e^{-\tau_{DN}}$ , respectively. The emissivity of the surface is modeled based on EIA, sea surface temperature, and wind speed with an emissivity model developed for HIRAD (El-Nimri et al. 2010). With this FRTM, TBs are modeled for the entire cross-track scene in increments of  $\sin^{-1}(\theta)$  in EIA. Those TBs are then weighted with HIRAD's antenna pattern to determine the observed TBs. Observed TB is calculated as

$$T_{B_{weighted_j}} = \sum_{i=1}^m T_{B_i} W_{ij}, \quad (4)$$

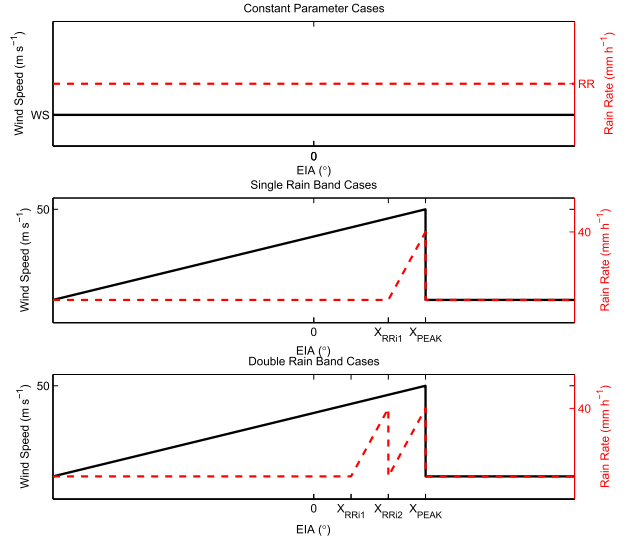


FIG. 4. Portrayals of the true surface wind speed ( $\text{m s}^{-1}$ ) and rain rate ( $\text{mm h}^{-1}$ ) used to simulate observations for each case type. The  $X$  parameters are labeled on the  $x$  axis to provide reference to Table 1 and are quantified in Table 1 for each test case identification (ID) number. Term  $X_{RRI1}$  is the horizontal distance to the point in the cross-track swath where the first (or only) rainband begins, from  $0^\circ$  EIA. Term  $X_{RRI2}$  is the distance to the point in the cross-track swath, from  $0^\circ$  EIA, where the second rainband begins (double-rainband cases only). Term  $X_{PEAK}$  is the distance to the point in the cross-track swath, from  $0^\circ$  EIA, where wind speed and the outer rainband peaks.

where  $T_{B_{weighted_j}}$  is the observed TB value at a particular cross-track location  $j$ ;  $T_{B_i}$  is the unweighted TB at a particular cross-track location  $i$ ; and  $W_{ij}$  is the normalized weight of the antenna pattern for the field of view at cross-track location  $j$ , at the same cross-track location of  $T_{B_i}$ . The number of cross-track positions is  $m$ . Examples of the antenna pattern at EIA =  $7^\circ$ ,  $36^\circ$ , and  $62^\circ$  are shown in Fig. 3. Also plotted in Fig. 3 is the halfpower beamwidth (HPBW). HPBW is the angle between points in the antenna pattern where the power is half of the maximum. With increasing EIA, HPBW increases.

### 3. Simulated observations as test cases

A set of simulated HIRAD observations was developed using the CPM FRTM in order to test the CPM algorithm. There are three main test case categories: horizontally uniform (or constant) conditions, a single rainband, and a double rainband. The test cases are summarized in Fig. 4 and Table 1. Figure 4 gives a visual glimpse of the cross-track scene in each case, while Table 1 outlines the case identification numbers and quantifies some of the parameters illustrated in Fig. 4.

Constant cases illustrate the performance of the CPM algorithm in different combinations of constant high and

TABLE 1. Summary of simulated test case identification numbers, and descriptions of the true surface wind speed ( $\text{m s}^{-1}$ ) and rain rate ( $\text{mm h}^{-1}$ ) for each case. The parameters of WS, RR,  $X_{\text{RR1}}$ ,  $X_{\text{RR2}}$ , and  $X_{\text{PEAK}}$  are labeled in Fig. 4 for a visualization of the types of cases simulated.  $X_{\text{RR1}}$  is the horizontal distance to the point in the cross-track swath where the first (or only) rainband begins, from  $0^\circ$  EIA.  $X_{\text{RR2}}$  is the distance to the point in the cross-track swath, from  $0^\circ$  EIA, where the second rainband begins (double rainband cases only).  $X_{\text{PEAK}}$  is the distance to the point in the cross-track swath, from  $0^\circ$  EIA, where wind speed and the outer rainband peaks. The identification numbers provide information about the particular test case. In the constant cases, the number before the “w” gives the true wind speed and the number before the “r” gives the true rain rate. In the rainband cases, the number before the letter “s” or “d” gives the EIA location of  $X_{\text{PEAK}}$ .

Constant cases: Constant wind speed/rain rate			
Test case ID	WS ( $\text{m s}^{-1}$ )	RR ( $\text{mm h}^{-1}$ )	
10w10r	10	10	
10w40r	10	40	
50w10r	50	10	
50w40r	50	40	
Single-rainband cases: Peak wind speed = $50 \text{ m s}^{-1}$ ; peak rain rate = $40 \text{ mm h}^{-1}$			
Test case ID	$X_{\text{RR1}}$ (km)	$X_{\text{PEAK}}$ (km)	
20s	3	7	
30s	7	10	
40s	10	15	
50s	15	21	
60s	21	31	
Double-rainband cases: Peak wind speed = $50 \text{ m s}^{-1}$ ; peak rain rate = $40 \text{ mm h}^{-1}$			
Test case ID	$X_{\text{RR1}}$ (km)	$X_{\text{RR2}}$ (km)	$X_{\text{PEAK}}$ (km)
20d	0	3	7
30d	3	7	10
40d	7	10	15
50d	10	15	21
60d	15	21	31

low retrieved parameters, where the retrieved parameters are surface wind speed and rain rate. The identification numbers in Table 1 give information about the amount of true wind speed and rain rate in that particular simulated test case. For the constant cases, the true wind speed is the number before the “w,” and the true rain rate is the number before the “r.” Figure 4 shows that the true wind speed and rain rate are held constant for the entire cross-track scene in the constant parameter test cases.

In addition to the constant parameter cases, idealized cases of a TC eyewall overpass—where the eyewall cuts through perpendicular to the cross-track view of the instrument—are also considered. The wind speed is assumed to linearly increase up to the location of the eyewall, followed by a drop in wind speed in the eye. Coinciding with the area of highest winds is an area of intense rainfall. Both single and double rainbands at the

eyewall are considered. The cross-track location of the eyewall is also an important feature to consider because the amount of coupling in the CPM FRTM is dependent on the cross-track location. Therefore, cases with different eyewall cross-track locations are considered.

Test cases with an “s” after the identification number in Table 1 have a single rainband, and cases with a “d” after the identification number have a double rainband. The identification number in these test cases corresponds to the EIA in HIRAD’s cross-track swath at which the eyewall peaks. For these cases, the wind speed peak value is always  $50 \text{ m s}^{-1}$  and the rain-rate peak value is always  $40 \text{ mm h}^{-1}$ . For convenience, Table 1 also includes approximate horizontal cross-track distances from  $0^\circ$  EIA that match these EIA points in the cross-track swath, labeled in Fig. 4.

## 4. Inversion algorithm

### a. Procedure

The FRTM is inverted using an iterative least squares estimator to retrieve surface wind speed and rain rate from HIRAD’s TB observations. To start, a first guess of wind speed and rain rate is estimated. The first guess is found by considering TBs with a range of wind speed and rain-rate pairs, and choosing the pair that results in the lowest difference between the observed and modeled TB. This procedure is performed for each cross-track pixel individually, using the DPM version of the FRTM. A uniform cross-track wind speed and rain-rate distribution is assumed as the first guess, with their values being the average of all the initial cross-track best guesses found.

With a first guess of wind speed and rain rate, the iteration process can start. Each iteration, a Jacobian matrix is populated using the FRTM for each retrieved value at each EIA as

$$J_{ij} = \frac{\partial T_{Bi}}{\partial g_j}, \quad (5)$$

where  $g$  is the wind speed or rain rate, the retrieved state variables. At the edge of the swath under the CPM assumption, we need to extend the Jacobian matrix to account for the extra downwelling atmosphere that extends past the surface pixel at the swath edge. This creates an  $m \times n$  matrix, where  $m$  is the number of cross-track TB observations and  $n$  is the sum of the number of wind speed and rain-rate retrievals for which they are being solved. In this CPM application,  $n$  is twice the number of pixels plus two, in order to account for the extra rain-rate retrievals attempted for the outer downwelling atmosphere at the edge of the swath. After  $\mathbf{J}$  is populated and beam averaging is accounted for, the update to the state vector is estimated as

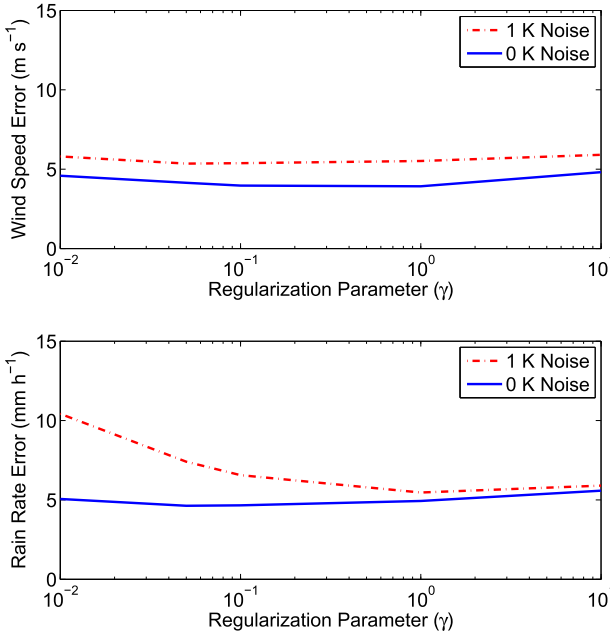


FIG. 5. The relationship between the amount of regularization and the corresponding errors in the retrieved (top) surface wind speed and (bottom) rain rate. The amount of error for each regularization amount represents an average across all simulated cases. For simulated cases with rainbands, errors were focused and averaged  $\pm 5^\circ$  EIA around the rainbands. Errors in the 1-K noise cases were averaged over 25 realizations of each simulated case for a representative idea of how random noise affects the retrieval performance at different levels of regularization.

$$\partial \mathbf{g} = (\mathbf{J}^T \mathbf{J} + \mathbf{R})^{-1} \mathbf{J}^T \partial \mathbf{T}_B, \quad (6)$$

where  $\mathbf{R}$  is a diagonal regularization matrix given by  $\mathbf{R} = \gamma \mathbf{I}$ , where  $\mathbf{I}$  is the identity matrix, and  $\partial \mathbf{T}_B$  is the vector of residual differences between the observed TB and the TB estimated by the FRTM given  $\mathbf{g}$ . The amount of regularization is determined by the regularization parameter  $\gamma$ .

The state vector  $\mathbf{g}$  is updated with  $\partial \mathbf{g}$  and this iterative process continues with the goal of minimizing the difference between the forward modeled TB and the observed TB. We define convergence when a decrease in the RMS value of  $\partial \mathbf{T}_B$  from one iteration to the next is less than 0.01 K, or if the RMS value increases. We determined the threshold value of 0.01 K after repeated experimentation with the algorithm. This threshold value, specific to these retrieval performance tests, insures that the run time for a retrieval is reasonable.

### b. Regularization issues

Regularization is used to decrease noise sensitivity in the inversion process. However, overregularization can have detrimental effects on the retrieval. We use the set of simulated test cases to determine a satisfactory value

for  $\gamma$ . Figure 5 shows the average error in retrieved wind speed and rain rate, over all simulated cases, for a range of  $\gamma$  values. We limit our investigation of errors to the portion of the cross-track  $\pm 5^\circ$  around the rainbands, for those cases with rainbands, in order to emphasize the performance of the retrieval near the rainbands more than the calmer portions of the scene.

The blue line in Fig. 5 represents the component of retrieval error not due to random additive noise (the so-called intrinsic error in the retrieval algorithm). The red line in Fig. 5 represents error due to noise sensitivity. Errors representing both components are based on the RMS difference between the true and retrieved values. The “intrinsic” error was calculated from retrievals that used simulated TBs with no added noise. To estimate the component of error due to noise sensitivity, 25 realizations of noisy simulated TBs were developed by adding random Gaussian noise with a standard deviation of 1 K to the noise-free simulated observations. One realization consists of a single set of cross-track TBs. Using those 25 realizations of noisy observations, 25 retrievals were performed. The error due to noise sensitivity is based on an average of those 25 realizations of noisy retrievals. The choice of 25 realizations was found to be adequate to produce repeatable results in a reasonable run time.

At low values of  $\gamma$ , sensitivity to noise is larger and contributes a significantly greater portion of the overall error. With  $\gamma$  above  $10^{-1}$ , the retrieval algorithm is overregularized, and we lose our ability to retrieve two distinct neighboring rainbands. Figure 6 compares retrievals of the noise-free simulated test cases 40s and 40d, and shows why a  $\gamma$  of  $10^{-1}$  was found to be the best choice for these tests. The solution that uses a  $\gamma$  equal to  $10^{-2}$  has too many ringing artifacts and will be too sensitive to noise. The ringing artifacts are oscillations versus EIA about the true value, which are caused by an underdamped inversion. The oscillations tend to increase with decreasing  $\gamma$ . Unfortunately, the CPM retrieval that uses a  $\gamma$  of  $10^0$  is unable to distinguish between the neighboring rainbands. A  $\gamma$  of  $10^{-1}$  is a good compromise between noise sensitivity and overregularization, and this  $\gamma$  value is used for the rest of the results reported.

## 5. Results

### a. Algorithm performance for simulated test cases

The CPM FRTM-based inversion algorithm with optimal regularization was applied to each of the simulated test cases to evaluate its performance. Table 2 gives the RMS difference (RMSD) between true and retrieved values for each retrieved parameter. For simplicity of comparison, these RMS values represent an average

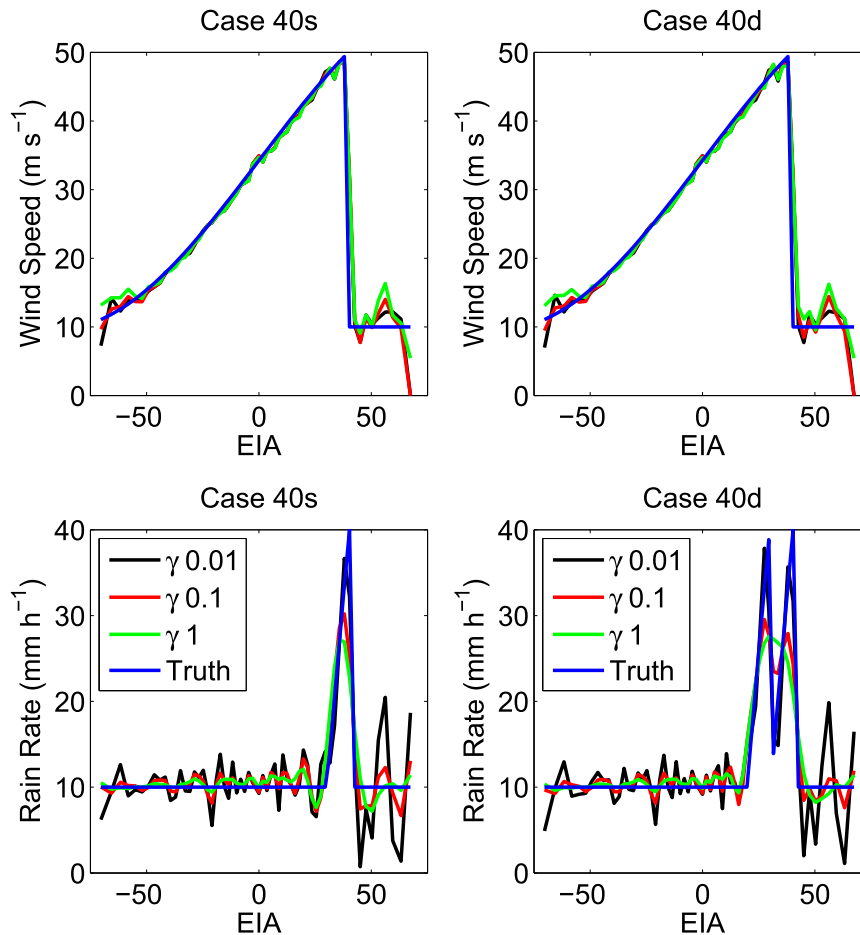


FIG. 6. Comparison of noise-free retrieval performance for simulated (left) case 40s and (right) case 40d over a range of  $\gamma$  values. A  $\gamma$  value of  $10^{-1}$  was chosen as a compromise value between a solution that is highly noise sensitive and a solution that cannot differentiate between two neighboring rainbands.

cross-track value for each test case. Performance was evaluated for simulated observations, with and without noise. For the observations with noise, we added random Gaussian distributed noise with a standard deviation of 1 K. We used 25 realizations of the 1-K noise tests to estimate the errors associated with the noisy retrievals.

The performance of the constant test cases are the most sensitive to noise because we chose a regularization parameter that worked best on average for all types of HIRAD situations. Sacrificing a noise-sensitive solution for the constant cases means that we are able to better resolve double-rainband-type situations. The retrieval performance with the constant test cases indicates fairly poor performances in the low-wind cases. This is likely due to low sensitivity of emissivity to wind speed under these conditions.

The retrieval performance in the single- and double-rainband cases indicates that, generally, performance degrades with a more complicated scene. Errors are

generally similar between the same cross-track position cases, but performance is dependent on the position of the eyewall. This is particularly true in the double-rainband case, where errors in rain-rate estimates increase with increasing EIA rainband position. Performance with the more complicated scenes can be degraded by both the antenna beam averaging and the cross-track coupling.

The relationship between cross-track coupling and EIA is illustrated in Fig. 7, which shows the correlation between errors in the wind speed and rain-rate retrievals. For each test case, the correlation was calculated for each position in the swath. Figure 7 shows the correlation across all test cases. A negative correlation exists along the main diagonal because wind speed and rain-rate retrievals at the same EIA tend to compensate for one another in order to minimize the overall error in the retrieval. The largest negatively correlated pixels represent the pixels in the field of view that have the

TABLE 2. RMSD between the true and CPM-retrieved parameters (averaged over the swath) for each test case simulation. Noise-free performance is listed under the 0-K noise columns. Noisy simulations were also tested with 25 realizations of observations with random Gaussian noise with a standard deviation of 1 K added. The RMSD for 1-K noise cases is an average value from the 25 realizations.

Test case ID	RMSD			
	Wind speed ( $\text{m s}^{-1}$ )		Rain rate ( $\text{mm h}^{-1}$ )	
	0-K noise	1-K noise	0-K noise	1-K noise
10w10r	1.7	5.3	1.3	3.8
10w40r	1.1	4.6	1.0	3.2
50w10r	0.5	1.7	0.7	3.5
50w40r	1.4	3.8	0.8	3.1
20s	2.6	4.6	2.3	5.5
30s	2.3	4.4	2.2	5.5
40s	3.2	4.7	2.5	5.5
50s	3.3	4.6	3.1	5.9
60s	2.2	3.9	2.9	6.0
20d	2.7	4.7	2.6	5.8
30d	2.4	4.1	3.0	5.7
40d	3.2	4.7	3.2	6.1
50d	3.2	4.5	4.1	6.3
60d	2.2	4.0	4.1	6.7

largest fractional contribution to the modeling of the atmosphere below the freezing level, and thus the rain rate in this field of view. Note that the negative correlation between wind speed and rain-rate errors at the same EIA has the potential to introduce compensating retrieval biases (e.g., wind speed too high and rain rate too low). In practice, this possibility can be monitored by independent ground truth validation of one or the other retrieved variable—typically the wind speed. This approach motivated the refinement of the rain absorption model used by SFMR, to correct for similar negatively correlated biases found in its wind speed retrievals at high rain rates (Klotz and Uhlhorn 2014).

Near nadir, there is much less coupling because the observing geometry at these locations is such that there is not a lot of crossover through neighboring columns of atmosphere. Farther away from nadir, there is a bit of asymmetry in the fields of view, as alluded to in Fig. 2b. The alternating negative and positive correlations are a consequence of the ringing artifacts that increase as the effects of cross-track coupling increase. At the edge of the swath, there is less coupling because the horizontal resolution of individual pixels increases enough to offset the larger EIAs.

*b. Algorithm performance for high-variability wind speed scenes*

While scenes with a double wind speed peak have not been observed with HIRAD, secondary wind maxima

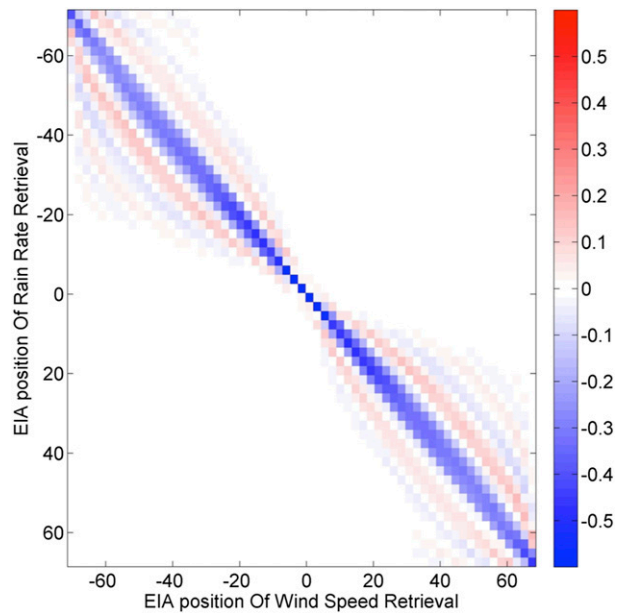


FIG. 7. Correlation between retrieval of rain rate and surface wind speed at one cross-track position with that at all other cross-track positions, composited over all simulated cases with 1-K noise. EIA is Earth incidence angle.

can occur during eyewall replacement cycles (Willoughby et al. 1982). The CPM algorithm is motivated by distinct rainbands occurring over small distances. The typical scales that motivated the development of the CPM

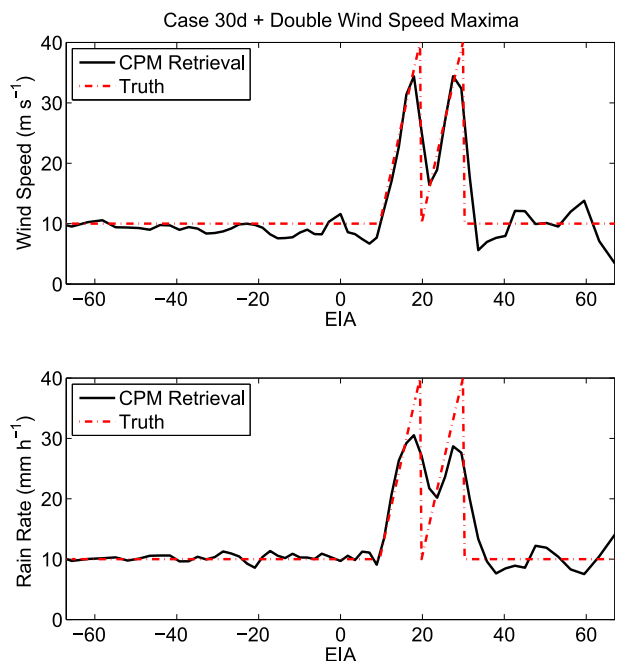


FIG. 8. An example of (top) wind speed and (bottom) rain rate CPM retrieval performance as compared to the simulation truth for a complicated and unusual double wind speed maxima and rainband scene.

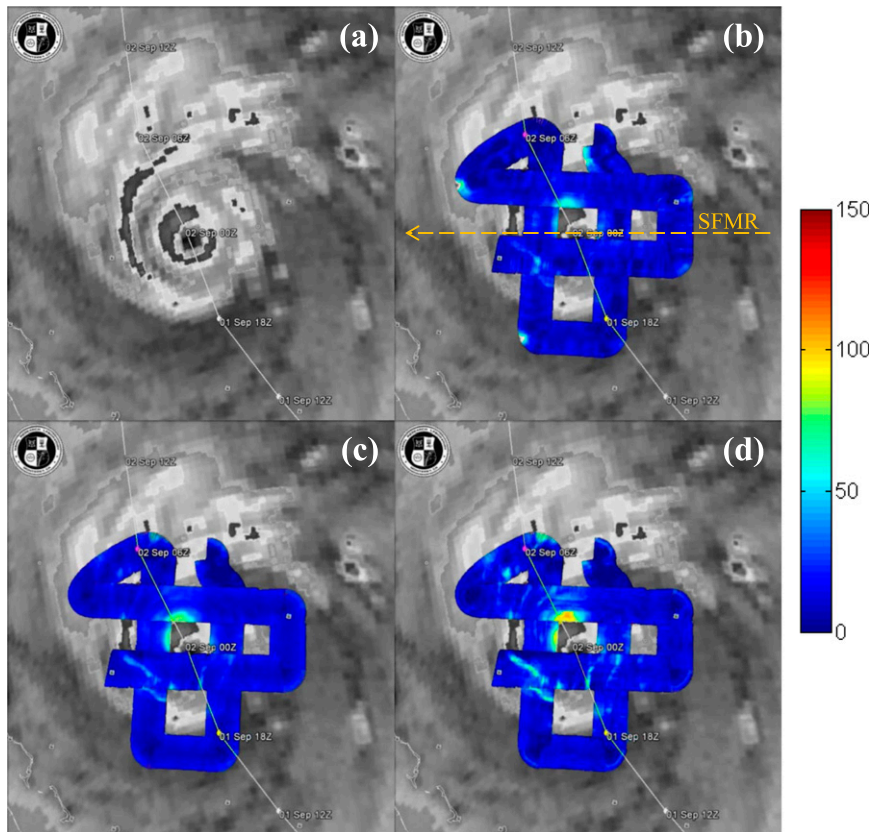


FIG. 9. HIRAD observations of Hurricane Earl (2010) during GRIP (color) and the closest 85-h satellite imagery (grayscale) from SSM/I. (a) The satellite imagery is shown alone. HIRAD observations are expressed as excess TB (K), which is (HIRAD observed TB – background TB), leaving only the relationships in TB due to strong winds and rain. (b) The approximate flight track of SEMR in addition to the excess TB at 4 GHz. (c) Excess TB for 5 GHz. (d) Excess TB for 6.6 GHz. The satellite imagery is courtesy of the Naval Research Laboratory.

algorithm are not typically seen for instances of secondary wind maxima. The double rainbands simulated in these performance tests were between 4 and 10 km from one another. During the eyewall replacement cycle, secondary wind maxima are seen closer to tens of kilometers from one another (Sitkowski et al. 2011). Even though these secondary wind maxima do not occur on the spatial scales that might be a problem for HIRAD, tests were completed that show what would happen if the cross-track wind speed scene were the same as the rain-rate scene simulated in the double rainband cases. An example of the double wind speed and rainband retrieval is shown in Fig. 8. The CPM algorithm can differentiate between both the double rainbands and the double wind speed peaks. RMSD values for these improbable wind speed scenes were found to be similar to the performance values of the double rainband test cases. While these scenes are improbable, the CPM model still performs well for these cases.

### c. Hurricane Earl (2010) HIRAD rain-rate retrievals

The CPM FRTM-based retrieval algorithm was applied to HIRAD observations of Hurricane Earl (2010) during the GRIP airborne campaign. Figure 9 shows HIRAD observations (color) along with near-simultaneous measurements of 85-GHz horizontally polarized (H-pol) TB by SSM/I on the *FI6* satellite platform (grayscale) observed at 2320 UTC 1 September 2010, hereafter referred to as 85-h satellite imagery. HIRAD's observations are shown in the form of excess TB (above that of a clear sky, calm ocean TB model) in order to emphasize the effects of wind speed and rain rate. The highest excess TBs are located where HIRAD passes over areas of intense rain and/or winds. Figure 9 shows that HIRAD tracked over the edges of the northern and western eyewalls, as well as a few of the outer rainbands.

Using the observations shown in Fig. 9, rain-rate and wind speed retrievals were performed. Figure 10 shows a

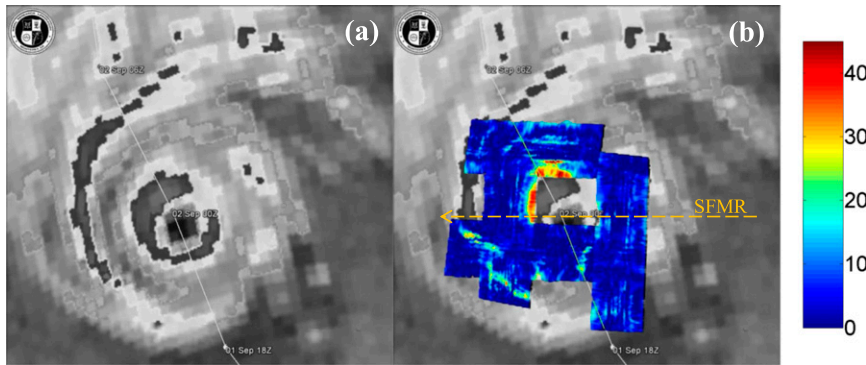


FIG. 10. (a) Shown is 85-h satellite imagery from SSM/I, courtesy of the Naval Research Laboratory. (b) A composite of HIRAD CPM rain-rate retrievals ( $\text{mm h}^{-1}$ ) of Hurricane Earl (2010) (color) and the closest 85-h satellite imagery (grayscale) from SSM/I. The dashed arrow shows the approximate flight track of SFMR.

composite of the rain rates retrieved. While there are some nonphysical artifacts of calibration in this image, the CPM algorithm–retrieved rain rates match up well to the 85-h satellite imagery. Both the outer and eyewall rainbands are captured at reasonable magnitudes and locations.

### 6. Discussion

#### a. Weighted antenna beam issues

In addition to being able to differentiate between the rain and wind signatures in the observations, the CPM algorithm is also able to partially deconvolve the averaging effects of the HIRAD antenna pattern. Figure 3 shows why convolution is an issue in HIRAD’s wide swath of observations. With increasing EIA, the antenna pattern’s HPBW increases. The CPM algorithm takes the beam averaging into account in the forward model and is therefore able to retrieve a solution that is closer to the truth than the beam-weighted scene. Figure 11 shows this performance capability in the context of test case 30d. While beam averaging will smooth out the scene variations, the retrieved wind and rain are more representative of the true wind and rain. Most importantly, the peak wind speed is captured alongside the two neighboring rainbands. After averaging the RMSD for all noise-free rainband cases, it was found that the CPM retrieval improves upon the beam-averaged truth for rain rate by  $0.3 \text{ mm h}^{-1}$  and for wind speed by  $2.3 \text{ m s}^{-1}$ .

#### b. Comparison of coupled and decoupled performance

The advantages of the CPM algorithm become most apparent at the outer edges of HIRAD’s cross-track swath. During GRIP, a similar instrument, SFMR, was flown on a NOAA P-3 at an altitude of around 3 km, with a track that allowed for nearly-collocated-with-HIRAD

observations of Hurricane Earl (2010). HIRAD was flown on a WB-57 at around 20 km. Figure 12 shows SFMR observations from an overpass of the western eyewall that were used to compare DPM- and CPM-based HIRAD rain-rate retrievals. These observations were located at nearly the same latitude and differ in time by about 15 min, at around 0000 UTC 2 September 2010.

Figure 12 shows that when a DPM FRTM–based retrieval algorithm is used, the algorithm is unable to resolve the two rainbands that SFMR observes in a similar location. However, the CPM retrieval is able to differentiate between these two rainbands and successfully retrieve them. The magnitudes of CPM rain-rate

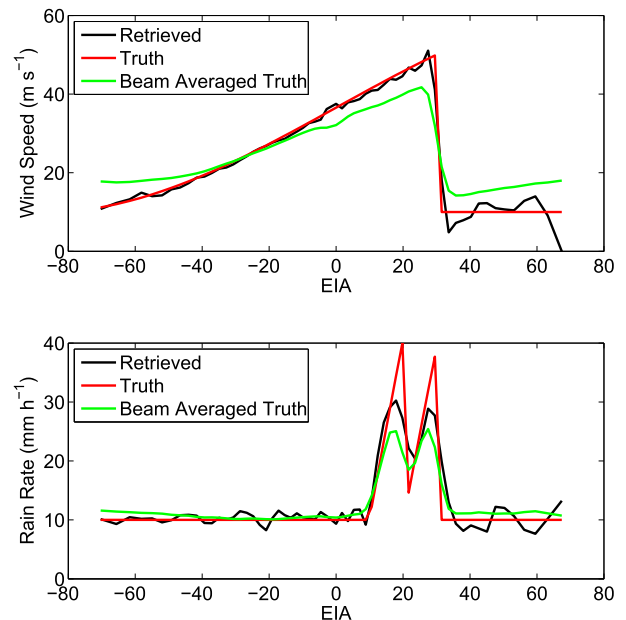


FIG. 11. (top) Wind speed and (bottom) rain-rate CPM retrieval performance as compared to the simulation truth and beam-averaged truth for case 30d.

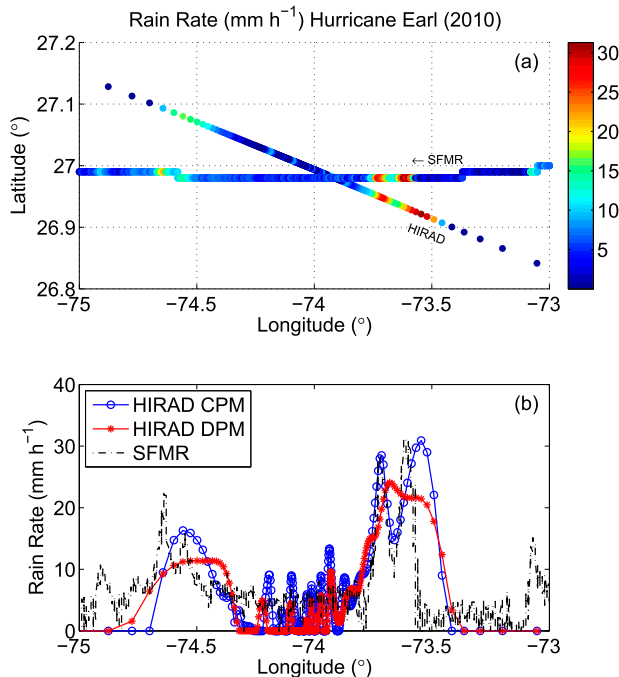


FIG. 12. (a) SFMR and HIRAD CPM-retrieved rain rate, plotted along the latitude and longitude coordinates for reference. Flying on different aircraft, SFMR and HIRAD observations differ in time by  $\sim 15$  min. (b) Plotted only with respect to longitude, a comparison of HIRAD rain-rate retrievals (using the decoupled and coupled-pixel algorithms), as compared to nearly collocated SMFR observations of Hurricane Earl (2010).

retrievals match up well with SFMR, and the location offset between their rainbands is likely due to slight differences in observation time and position.

The HIRAD absolute calibration errors are large enough that its wind speed retrievals are still problematic and are therefore not shown in Fig. 12. Rain-rate retrievals are found to be much less sensitive to the absolute calibration issues; this results because the rain-rate retrieval depends on differences between TB at different frequencies rather than on the absolute TB level. With well-calibrated observations, the wind speed can be estimated too, as has been shown by the simulations presented here.

### c. Other applications

As remote sensing technology advances, the CPM method could be valuable in spaceborne applications as well. Atmospheric phenomena exhibiting high gradients across a scene could pose retrieval challenges similar to HIRAD's challenges if the field of view cuts through a high-gradient scene with high resolution. For example, narrow bands of moisture called atmospheric rivers (ARs) could potentially satisfy these high-gradient scene requirements. ARs provide the West Coast of the United States with extreme precipitation (Guan

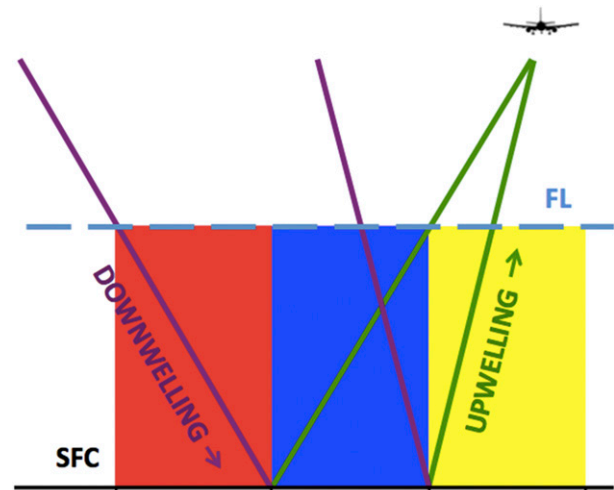


FIG. A1. This diagram shows a simple example, where three atmospheric columns contribute toward a single field of view, each having potentially different rain amounts, designated by the red, blue, and yellow values, respectively. The upwelling propagation path, signified by the green line, intersects through the blue and yellow columns of atmosphere. The downwelling propagation path, signified by the purple line, intersects through the red and blue columns of atmosphere. FL stands for freezing level. SFC stands for the ocean surface.

et al. 2010). High-gradient scenes like this could pose challenges for advanced sensors of the future.

## 7. Conclusions

While developing a physically based retrieval algorithm for HIRAD, we found that the simplifying assumptions commonly used in spaceborne applications and with HIRAD's heritage instrument, SFMR, were not always acceptable for HIRAD. This led to the development of a more robust method, the CPM algorithm. The CPM is different from the DPM previously used because it allows for the possibility that a single column of atmosphere can affect the observations along multiple cross-track positions. High-contrast rain features, such as those that occur in an eyewall, can now be properly accounted for because there is no longer an assumption that the upwelling and downwelling atmospheric emission originate from the same atmospheric column. Using the CPM algorithm, HIRAD can differentiate between two neighboring rainbands, whereas the DPM algorithm cannot. Although the performance of this algorithm is limited by the beamwidths at the edge of HIRAD's swath, the algorithm is also able to partially deconvolve the beam-averaged observations, getting closer to the truth. HIRAD's observations and retrieval algorithm remain a work in progress, but strides are being made to improving its reliability. The favorable

TABLE A1. The number of rain pixels that are considered when calculating the effective rain rate in the field of view at EIA of the subset of observations used in the simulated test case setup.

EIA	No. of rain pixels
0	1
2	3
4	3
5	3
7	4
9	5
11	5
12	5
14	6
16	7
18	7
20	7
22	7
24	8
26	8
27	8
29	8
32	8
34	8
36	8
38	8
40	8
43	8
45	8
48	8
50	8
53	7
56	7
60	6
63	6
67	4

performance of the CPM has only been demonstrated thus far by the case studies presented here. Future work will include the assessment of performance in more cases as they become available with future airborne campaigns.

*Acknowledgments.* The authors gratefully acknowledge the contributions and support provided by the HIRAD science and engineering teams at NASA Marshall Space Flight Center, NOAA, and the University of Central Florida. In particular, Sayak Biswas and Spencer Farrar provided HIRAD and SFMR data. The work reported here was supported in part by Award NNX11AK17G with the NASA Marshall Space Flight Center.

## APPENDIX

### Derivation of Interpixel Coupling Weights in the CPM

The CPM FRTM requires individual estimates of the path-integrated optical depth along each of the

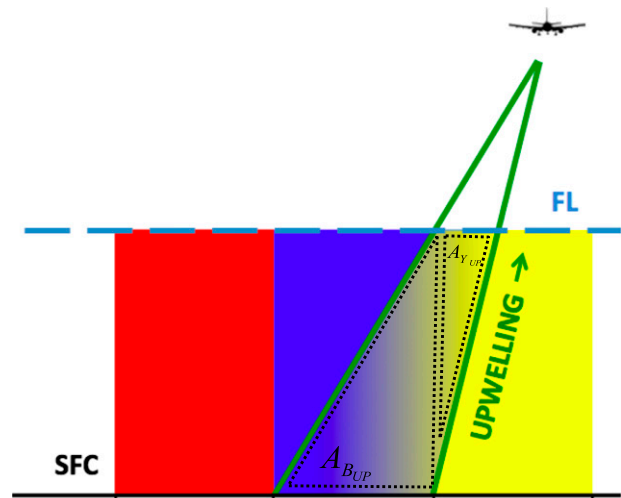


FIG. A2. This figure illustrates that the weighted upwelling rain rate would be a weight of the blue and yellow columns of atmosphere. Terms  $A_{YUP}$  and  $A_{BUP}$  are labeled for reference to (A1).

upwelling and downwelling propagation paths of the measured brightness temperature at each pixel in the HIRAD wind speed image. The estimates are made using the following model for the atmosphere. Below the freezing level, a vertically uniform rain column is assumed to exist down to the surface. It is also assumed to be uniform horizontally across each surface pixel over which the wind speed is estimated. The optical depth of a rain column is assumed to scale linearly with its rain rate. The appropriate scale factor ( $Np\text{ mm}^{-1}\text{ h}$ ) is given in [Amarin \(2010\)](#). The total path-integrated optical depth through the rain is found by breaking the path up into segments that pass through the rain column above each surface pixel. [Figure A1](#) shows an example of an observing geometry in which the propagation path passes through the rain column above three surface pixels. The number of distinct rain columns intersected will vary, depending on the subset of observations used and the EIA of the surface pixel considered, with higher EIAs crossing through more columns. [Table A1](#) shows, as a function of EIA, the number of distinct rain columns that must be considered when computing the total path-integrated optical depth in the setup used for the simulated test cases. At nadir, it is sufficient to consider only the single rain column above the surface pixel under observation. In this case, the CPM reduces to the DPM FRTM. At high EIA values, near the swath edge, there is significant coupling between rain columns over many surface pixels on either side of the surface pixel under observation. At the outermost edge of the swath, the horizontal resolution of the rain columns degrades, causing the number of pixels to decrease slightly compared to

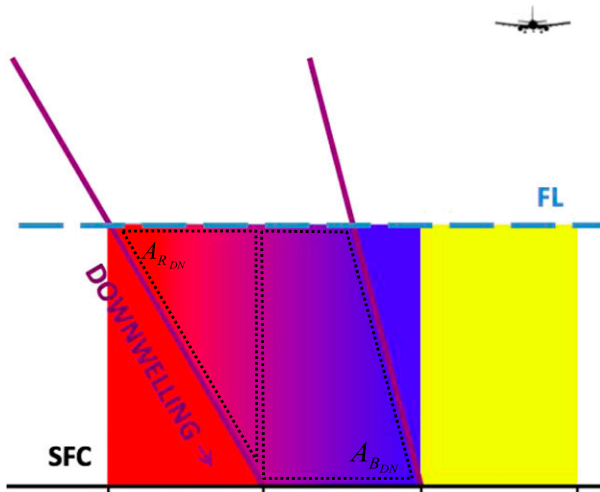


FIG. A3. This figure illustrates that the weighted downwelling rain rate would be a weight of the blue and red columns of atmosphere. Terms  $A_{R_{DN}}$  and  $A_{B_{DN}}$  are labeled for reference to (A2).

the peak amount of coupling considered in the middle edge of the swath.

The total effective rain rate along a propagation path, from which the optical depth is derived, is the weighted average of the rain rates of all rain columns intersected. The appropriate weighting is found geometrically. In the example in Fig. A2, the rain rate integrated along the upwelling propagation path is a weighted average of the rain in the yellow and blue columns, as given by

$$R_{UP} = \frac{A_{B_{UP}} R_B + A_{Y_{UP}} R_Y}{A_{B_{UP}} + A_{Y_{UP}}}, \quad (\text{A1})$$

where  $R_Y$  is the rain rate in the yellow column,  $R_B$  is the rain rate in the blue column,  $A_{Y_{UP}}$  is the area of the yellow upwelling polygon below the freezing level, and  $A_{B_{UP}}$  is the area of the blue upwelling polygon below the freezing level.

Similarly, the rain rate integrated along the downwelling propagation path is a weighted average of the rain in the red and blue columns shown in Fig. A3, or

$$R_{DN} = \frac{A_{B_{DN}} R_B + A_{R_{DN}} R_R}{A_{B_{DN}} + A_{R_{DN}}}, \quad (\text{A2})$$

where  $R_B$  is the rain rate in the blue column,  $R_R$  is the rain rate in the red column,  $A_{R_{DN}}$  is the area of the downwelling red polygon below the freezing level, and  $A_{B_{DN}}$  is the area of the downwelling blue polygon below the freezing level.

Once the total effective rain rate has been computed along both the upwelling and downwelling propagation

paths, the corresponding optical depths can be computed. These are then used in the CPM FRTM, as explained in section 2.

## REFERENCES

- Amarin, R. A., 2010: Hurricane wind speed and rain rate measurements using the airborne Hurricane Imaging Radiometer (HIRAD). Ph.D. dissertation, University of Central Florida, 171 pp. [Available online at [http://etd.fcla.edu/CF/CFE0003082/Amarin\\_Ruba\\_A\\_201005\\_PhD.pdf](http://etd.fcla.edu/CF/CFE0003082/Amarin_Ruba_A_201005_PhD.pdf).]
- , W. L. Jones, S. F. El-Nimri, J. W. Johnson, C. S. Ruf, T. L. Miller, and E. Uhlhorn, 2012: Hurricane wind speed measurements in rainy conditions using the airborne Hurricane Imaging Radiometer (HIRAD). *IEEE Trans. Geosci. Remote Sens.*, **50**, 180–192, doi:10.1109/TGRS.2011.2161637.
- Braun, S. A., and Coauthors, 2013: NASA's Genesis and Rapid Intensification Processes (GRIP) field experiment. *Bull. Amer. Meteor. Soc.*, **94**, 345–363, doi:10.1175/BAMS-D-11-00232.1.
- El-Nimri, S. F., W. L. Jones, E. Uhlhorn, C. Ruf, J. Johnson, and P. Black, 2010: An improved C-band ocean surface emissivity model at hurricane-force wind speeds over a wide range of Earth incidence angles. *IEEE Geosci. Remote Sens. Lett.*, **7**, 641–645, doi:10.1109/LGRS.2010.2043814.
- Guan, B., N. P. Molotch, D. E. Waliser, E. J. Fetzer, and P. J. Neiman, 2010: Extreme snowfall events linked to atmospheric rivers and surface air temperature via satellite measurements. *Geophys. Res. Lett.*, **37**, L20401, doi:10.1029/2010GL044696.
- Klotz, B. W., and E. W. Uhlhorn, 2014: Improved Stepped Frequency Microwave Radiometer tropical cyclone surface winds in heavy precipitation. *J. Atmos. Oceanic Technol.*, **31**, 2392–2408, doi:10.1175/JTECH-D-14-00028.1.
- Kummerow, C., W. S. Olson, and L. Giglio, 1996: A simplified scheme for obtaining precipitation and vertical hydrometeor profiles from passive microwave sensors. *IEEE Trans. Geosci. Remote Sens.*, **34**, 1213–1232, doi:10.1109/36.536538.
- Nordberg, W., J. Conaway, D. B. Ross, and T. Wilheit, 1971: Measurements of microwave emission from a foam-covered, wind-driven sea. *J. Atmos. Sci.*, **28**, 429–435, doi:10.1175/1520-0469(1971)028<0429:MOMEFA>2.0.CO;2.
- Prabhakara, C., G. Dalu, G. L. Liberti, J. J. Nucciarone, and R. Suhasini, 1992: Rainfall estimation over oceans from SSMR and SSM/I microwave data. *J. Appl. Meteor.*, **31**, 532–552, doi:10.1175/1520-0450(1992)031<0532:REOOPS>2.0.CO;2.
- Rosenkranz, P. W., and D. H. Staelin, 1972: Microwave emissivity of sea foam and its effect on nadir radiometric measurements. *J. Geophys. Res.*, **77**, 6528–6538, doi:10.1029/JC077i033p06528.
- Sitkowski, M., J. P. Kossin, and C. M. Rozoff, 2011: Intensity and structure changes during hurricane eyewall replacement cycles. *Mon. Wea. Rev.*, **139**, 3829–3847, doi:10.1175/MWR-D-11-00034.1.
- Stephens, G. L., and C. D. Kummerow, 2007: The remote sensing of clouds and precipitation from space: A review. *J. Atmos. Sci.*, **64**, 3742–3765, doi:10.1175/2006JAS2375.1.
- Stogryn, A., 1967: The apparent temperature of sea at microwave frequencies. *IEEE Trans. Antennas Propag.*, **15**, 278–286, doi:10.1109/TAP.1967.1138900.
- Uhlhorn, E. W., and P. G. Black, 2003: Verification of remotely sensed sea surface winds in hurricanes. *J. Atmos. Oceanic Technol.*, **20**, 99–116, doi:10.1175/1520-0426(2003)020<0099:VORSSS>2.0.CO;2.
- , —, J. L. Franklin, M. Goodberlet, J. Carswell, and A. S. Goldstein, 2007: Hurricane surface wind measurements from

- an operational Stepped Frequency Microwave Radiometer. *Mon. Wea. Rev.*, **135**, 3070–3085, doi:10.1175/MWR3454.1.
- Weinman, J., and P. Guetter, 1977: Determination of rainfall distributions from microwave radiation measured by the Nimbus 6 ESMR. *J. Appl. Meteor.*, **16**, 437–442, doi:10.1175/1520-0450(1977)016<0437:DORDFM>2.0.CO;2.
- Wilheit, T. T., 1976: Meteorological interpretations of the images from the Nimbus 5 Electronically Scanned Microwave Radiometer. *J. Appl. Meteor.*, **15**, 166–173, doi:10.1175/1520-0450(1976)015<0166:MIOTIF>2.0.CO;2.
- , 1986: Some comments on passive microwave measurement of rain. *Bull. Amer. Meteor. Soc.*, **67**, 1226–1232, doi:10.1175/1520-0477(1986)067<1226:SCOPMM>2.0.CO;2.
- , and Coauthors, 1994: Algorithms for the retrieval of rainfall from passive microwave measurements. *Remote Sens. Rev.*, **11**, 163–194, doi:10.1080/02757259409532264.
- Willoughby, H. E., J. A. Clos, and M. G. Shoreibah, 1982: Concentric eyewalls, secondary wind maxima, and the evolution of the hurricane vortex. *J. Atmos. Sci.*, **39**, 395–411, doi:10.1175/1520-0469(1982)039<0395:CEWSWM>2.0.CO;2.